Chapter 6. Stage-2 Components

6.1 Superconducting Magnet Systems

The application of superconductivity for high-energy accelerators started more than 20 years ago. At the present time four machines, the Tevatron (FNAL), HERA (DESY), NUKLOTRON (JINR) and RHIC (BNL) are in operation, and LHC (CERN) is under construction. All these machines utilize NbTi superconducting (SC) magnets cooled by LHe at a nominal temperature of 1.9 or 4.5 K. NbTi has an upper critical magnetic field of 14-15 T at 0 K (10 T at 4.2 K) and a critical temperature of 9.5 K. Thanks to the excellent mechanical properties of NbTi, traditional electromagnet technologies could be used in the construction of these magnets. Accelerator dipole magnets based on this technology provide 7.5-8 T maximum field (6-7 T operating field) at 4.5 K and the 10-10.5 T maximum field (8-9 T operating field) at 1.9 K of the required field quality. These magnets behave reliably and reproducibly in thermal and current cycles over long periods of time in hard radiation environments. Thousands of short and full-scale (6-15 m long) NbTi magnets have been fabricated, tested and used in large accelerator/collider projects, beginning with the Tevatron, and continuing through RHIC and LHC. The technology of NbTi magnets has been successfully demonstrated in mass production in industry (HERA, RHIC) at affordable costs. Although NbTi can be used in Stage-2 for relatively low-field magnets such as multipole correctors, NbTi magnets do not reach the nominal field of 10 T chosen for the main arc dipoles.

Alternative superconductors for high field accelerator magnets are the A15 materials, Nb_3Sn in particular. Nb_3Sn has a high upper critical magnetic field of 23-24 T at 4.2 K and a critical temperature of 18 K. It is produced commercially on a fairly large scale. Formation of the Nb_3Sn phase and its properties (brittleness) determine two possible approaches to magnet fabrication: wind-and-react or react-and-wind techniques. Nb_3Sn accelerator magnets employing different coil designs and utilizing both wind-and-react and react-and-wind fabrication techniques are being investigated at various U.S. and European HEP laboratories and universities [1–7]. In the past 5-8 years, magnetic fields above 10 T have been achieved. The magnet group at Twente University (Netherlands) achieved 11 T at 4.3 K with a two-layer cos-theta dipole model [8]. The LBNL group built a four-layer cos-theta dipole model that reached fields above 12.4 T at 4.3 K and above 13 T at 1.9 K [9]. A common coil Nb_3Sn racetrack structure at LBNL recently reached 12 T field at 4.2 K [10]. Progress in raising the critical current of Nb_3Sn strands [11] and in developing magnet technologies for brittle superconductors make it possible to design *cost-effective* Nb_3Sn accelerator magnets with a nominal field of 10-12 T. Although only a few short models have been fabricated and tested up to now, the positive results of this work make Nb_3Sn conductor very attractive for Stage-2 magnets.

Since the construction of Stage 2 is many years from now, new emerging SC materials and technologies could be considered in the future. The most promising of the new materials include $Bi_2Sr_2CaCu_2O_x$ (BSCCO-2212), with T_c ~85 K, and $Bi_2Sr_2Ca_2Cu_3O_x$ (BSCCO-2223), having T_c ~110 K. Kilometer-length quantities of these materials have been made in the form of multifilamentary tapes or round strands, suitable for a magnet

using the flat racetrack coil design [11]. Another material, YBCO, shows even more promising properties. Very high critical current densities have been achieved at high fields in YBCO short samples. However, commercial production of this material lags well behind BSCCO. An appropriate magnet technology for this material has yet to be invented. Cost of all HTS materials is very high and their production rate is too low at the present time to be considered for Stage-2 magnets. In small quantities these materials could be used for special Stage-2 magnets required in both Stage 1 and Stage 2, such as the interaction region (IR) magnets.

6.1.1 Stage-2 Magnet System

The Stage-2 magnet system consists of SC arc dipoles, quadrupoles and corrector magnets as well as special SC magnets such as dispersion suppression magnets, IR magnets, and special correctors. A discussion of magnet field quality and tolerances is presented in Section 3.3.

Based on the chosen lattice and machine operation parameters, Stage-2 arc magnets should meet the following general requirements:

- operation field range 1-10 T for arc and DS dipole magnets
- field gradient range 45-400 T/m for arc and DS quadrupole magnets
- good field quality in the operational range
- coil aperture ≥40 mm, sufficient for installation of the vacuum chamber and beam screen
- vertical bore arrangement
- operation temperature range 4.5-5.5 K
- sufficient critical current and critical temperature margin for reliable operation under high heat load from synchrotron radiation
- restricted temperature and voltage change during a quench
- robust mechanical design at affordable magnet cost

Proton beams in Stage 2 circulate in opposite directions in two crossing storage rings. These storage rings can be designed based on single-aperture magnets placed in separate cryostats (SSC) [12] or based on double-aperture magnets with common iron yoke and cryostat (LHC) [13]. The second approach allows reducing the size, weight and cost of magnet and cryostat. Since all these parameters are important for the VLHC, this approach was chosen for the Stage-2 high field magnets.

6.1.2 Arc Dipole Magnets

The arc dipoles use a cold yoke design based on the common coil approach. The design meets the Stage-2 VLHC requirements.

Flat racetrack coils are shared between two vertically positioned apertures. The common coil dipole design described here is a simple single-layer coil divided into three blocks by wide spacers. This simplifies design and fabrication technology, and allows the possibility of using reacted brittle Nb_3Sn cable, solving many mechanical problems, and at the same time achieving excellent field quality [14].

The coils are made of rectangular Rutherford-type cable with 60 Nb_3Sn strands, each 0.7 mm in diameter. The bare cable width is 22.22 mm and the thickness is 1.250 mm. The insulation is 0.10 mm thick and made of fiberglass tape.

Each coil consists of 58 turns grouped into three blocks and separated by 6 mm thick spacers. There are also two 3 mm thick spacers in each middle block. The pole blocks are shifted horizontally inwards by 5 mm with respect to the middle blocks. The size and position of blocks and spacers were optimized to provide the maximum transfer function, minimum coil volume and small low-order geometrical harmonics within the largest possible gap. The gap between pole blocks is 40 mm, determining the magnet aperture. The use of the reacted Nb_3Sn cable dictates a minimum bending radius of 90 mm for the chosen strand size and thus sets the aperture separation to 290 mm.

The iron yoke is split vertically into two pieces. To provide contact between the collared coil and the yoke at all temperatures, the gap between yoke pieces is always open. Special holes are used for correction of iron saturation. The yoke inner surface and outer radius, geometry and position of the correction holes were optimized to provide good field quality, low fringe fields, maximum transfer function and smallest yoke size. Figure 6.1 shows the flux distribution in a 2D cross-section of the arc dipole. A top/bottom yoke asymmetry relative to the magnet aperture will cause a skew quadrupole component in the case of symmetric coils. This component was reduced using a small top/bottom block asymmetry with respect to the mid-plane of each aperture.

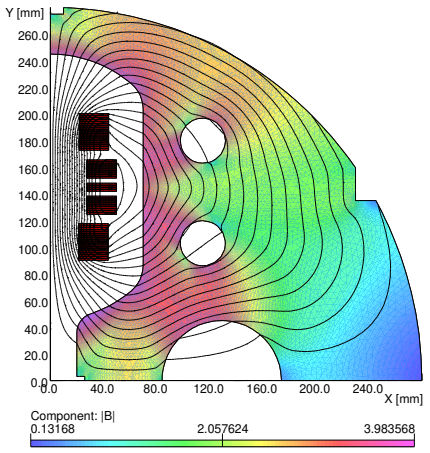

Figure 6.1. Magnetic design of the arc dipole.

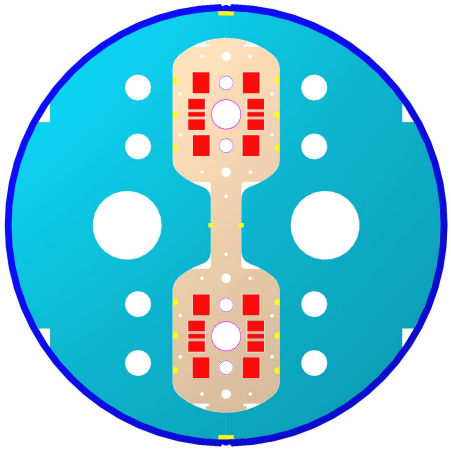

Figure 6.2. Cross-section of the arc dipole.

This design allows the use of a stress management strategy. Coil blocks, surrounded by the 0.5 mm thick electrical insulation, are placed inside a strong collar structure. The collar structure has round holes for the beam pipe and the cooling channels. During assembly the collar structure provides the vertical prestress and protects the coil from the horizontal and vertical over-compression. During operation it prevents an accumulation of the vertical Lorentz forces and a force transfer from the pole blocks to the mid-plane blocks. It also intercepts a significant part of the horizontal Lorentz forces reducing stresses in the yoke and skin. At all conditions, stress in the coil is less than 150 MPa, which is safe for the Nb_3Sn cable [15].

Both coils are wound directly into the support structure and impregnated with epoxy. The collared coil assembly is placed inside the iron yoke surrounded by a 10 mm thick stainless steel skin. Thick end plates welded to the skin restrict the longitudinal motion of the coils. The horizontal pre-compression of the collared coil is provided by the stainless steel skin via the iron yoke. The main calculated parameters are summarized in Table 6.1, and the 2D cross-section of the magnet cold mass is shown in Figure 6.2.

Table 6.1. Arc dipole parameters.

B_{nom}, T	10
I_{nom}, kA	23.5
Aperture, mm	40
Aperture separation, mm	290
Magnetic length, m	16.15
Iron yoke OD, mm	560
Stored energy @10T, kJ/m	2×414
Inductance @10T, mH/m	2×1.5

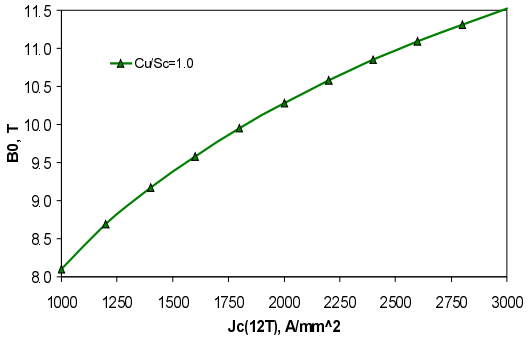

Figure 6.3. Arc dipole short sample limit.

Maximum (quench) field in the magnet aperture at 4.2 K vs. the critical current density of SC strand in the coil is shown in Figure 6.3. At 15% I_c degradation [16,17], a nominal field of 10 T with 10% margin will be achieved using the new Nb_3Sn strands with $J_c(12T,4.2K) = 3$ kA/mm^2 [18].

The magnetic field in the dipole bore is described according to the expression

$$B_y + iB_x = B_0 \sum_{n=1}^{\infty} [b_n + ia_n] \cdot \left(\frac{z}{R_{ref}} \right)^n .$$

Calculated geometrical harmonics and their RMS spread at 1 cm radius for ±50 μm random coil block displacements for the arc dipole are shown in Table 6.2.

Table 6.2. Relative dipole systematic and random geometrical harmonics at 1 cm radius, 10^{-4}.

Harmonic number, n	Systematic, b_n	Systematic, a_n	RMS ($\sigma_{a,b}$)
1	-	0.003	1.040
2	0.000	-	0.360
3	-	-0.005	0.141
4	0.001	-	0.046
5	-	+0.002	0.017
6	0.001	-	0.006
7	-	0.010	0.003
8	-0.026	-	0.002
9	-	0.002	0.000

The effect of iron saturation on the magnet transfer function and low order field harmonics is shown in Figure 6.4. The coil magnetization effect is shown in Figure 6.5. The reduction of the dipole transfer function at the nominal field of 10 T is about 9.2%. The iron saturation effect on the low order harmonics in the operating field range 1-10 T is effectively suppressed by optimizing the yoke size and correction hole geometry. The coil magnetization effect at B>1 T is small even with the currently availble Nb_3Sn strands having a large effective filament diameter of ~100 μm [19].

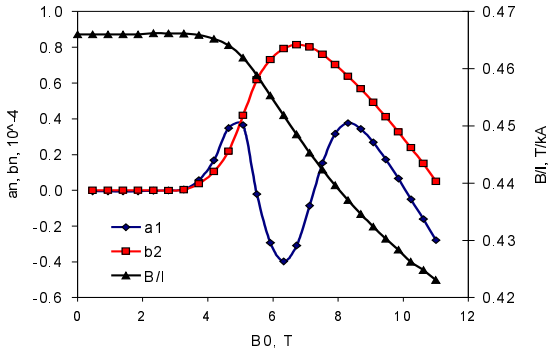

Figure 6.4. Iron saturation effect.

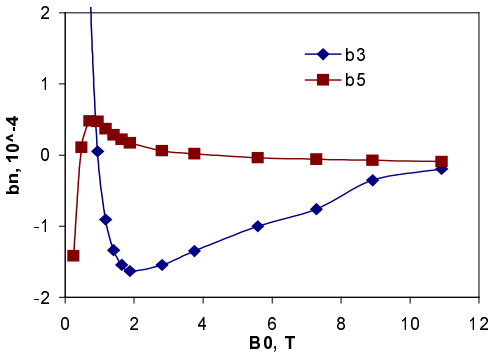

Figure 6.5. Coil magnetization effect.

6.1.3 Arc Quadrupole Magnets

The 2-in-1 arc quadrupole magnet design with vertical bore arrangement and FF or DD functions [20] was developed to use together with the arc dipole magnet described above. The magnet design is based on a two-layer shell-type coil and cold iron yoke, and meets the Stage-2 requirements.

The coil bore diameter is 43.5 mm. Each coil quadrant consists of 13 turns. The inter-layer spacer is 0.28 mm thick and the additional mid-plane insulation layers are 2×0.125 mm thick. Each coil quadrant has a floating pole and two wedges in the inner layer in order to minimize low order field harmonics. Coil ends have a block-wise layout of turns optimized to reduce the maximum field in the ends and to improve end field quality.

The coil utilizes a keystone Rutherford-type cable made of 28 Nb_3Sn strands, each 1 mm in diameter. The bare cable width is 14.24 mm, the thickness is 1.800 mm and the keystone angle is 0.91 degree. The cable is wrapped with special insulation suitable for the long high-temperature heat treatment. The nominal thickness of the cable insulation is 0.25 mm. Both layers of half-coil are made from one cable piece without an inter-layer splice.

Two collared coils are placed in 144 mm diameter circular holes separated by 290 mm inside the common iron yoke. Special holes are used for correction of iron saturation. The iron yoke was split vertically into two pieces to allow assembly of two coils in one yoke. In order to reduce the effect of gap variation on the field quality, the vertical gap between the two iron pieces is always closed. Figure 6.6 shows the flux distribution in the optimized 2D cross-section of the arc quadrupole magnet.

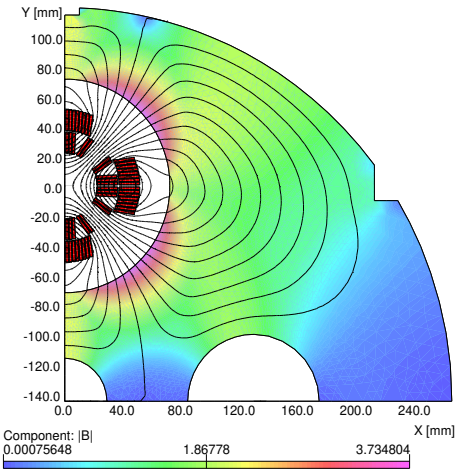

Figure 6.6. Arc quadrupole magnetic design.

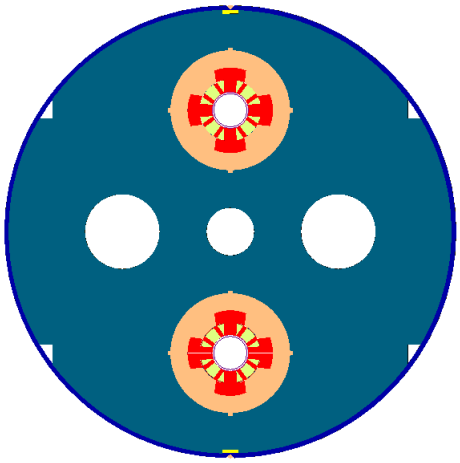

Figure 6.7. Arc quadrupole cross-section.

The magnet body is prestressed and mechanically supported by means of stainless steel collar laminations. Tapered keys lock collar laminations in two perpendicular directions. Thick aluminum end cans provide prestress and mechanical support of the coil ends. Coil prestress is less than 150 MPa in all conditions [21].

The collared coil is centered inside the yoke with the help of alignment keys. No additional radial support from the iron yoke is required. The yoke outer diameter is 530 mm. Yoke laminations feature large round holes for LHe flow and special cutouts required for precise alignment. The two-piece iron yoke is enclosed by a 6 mm thick stainless steel skin. To restrict coil longitudinal motion, two thick stainless steel end plates are welded onto the skin. The cross-section of the arc quadrupole is shown in Figure 6.7. The main calculated parameters are summarized in Table 6.3.

Table 6.3. Arc quadrupole parameters..

G_{nom}, T/m	400
I_{nom}, kA	27.2
Aperture, mm	43.5
Aperture separation, mm	290
Magnetic length, m	9.16
Iron yoke OD, mm	530
Stored energy @400T/m, kJ/m	2×209
Inductance @400T/m, mH/m	2×0.57

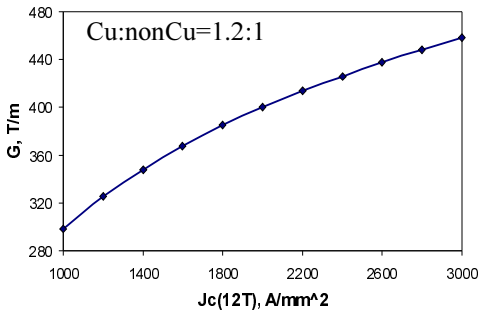

Figure 6.8. Arc quad short sample limit.

Maximum (quench) field gradient in the magnet aperture at 4.2 K vs. the critical current density of Nb_3Sn strand in the coil is shown in Figure 6.8. Assuming 10% I_c degradation [16], a nominal gradient of 400 T/m with 10% margin will be achieved using R&D Nb_3Sn strands with J_c(12T, 4.2K) = 3 kA/mm^2 [18]. Calculated geometrical harmonics and

their rms spread at 1-cm radius for ±50 μm random coil block displacements for the arc quadrupole are summarized in Table 6.4.

Table 6.4. Quadrupole systematic and random geometrical harmonics at 1-cm radius, 10^{-4}.

Harmonic number, n	Systematic, b_n	Systematic, a_n	rms, $\sigma_{a,b}$
2	-	-	1.82
3	-	-	0.82
4	-	-	0.38
5	-0.0003	-	0.19
6	-	-	0.07
7	-	-	0.026
8	-	-	0.013
9	-0.0039	-	0.001

The effect of iron saturation at high fields on the magnet transfer function and low order field harmonics is shown in Figure 6.9. The coil magnetization effect is shown in Figure 6.10.

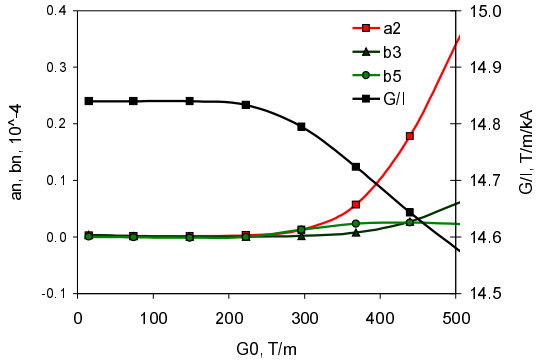

Figure 6.9. Iron saturation effect.

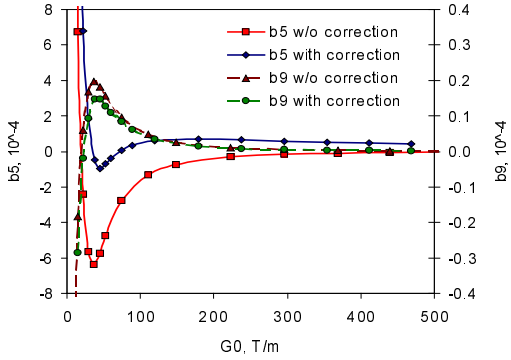

Figure 6.10. Coil magnetization effect.

Reduction of the quadrupole transfer function at the nominal field gradient of 400 T/m is about 1%, smaller than the reduction of the dipole transfer function. To provide a constant G/B ratio in the operation field range, the arc quadrupole magnets will be powered independently from the arc dipole magnets. The iron saturation effect on the normal and skew low order harmonics at field gradient G<400 T/m is effectively suppressed by optimizing the yoke size and correction hole geometry. The coil magnetization effect at G>45 T/m is minimized using a simple passive correction system based on iron strips [22]. Additional reduction will be achieved by reducing the effective filament diameter in Nb_3Sn strands.

6.1.4 Arc Corrector Magnets

The correction system required for Stage-2 consists of two subsystems: an arc correction system and an IR correction system. This section describes the correction magnets to be used in the arc, including the dispersion suppressor regions. The arc correction system includes dipole, quadrupole and sextupole correctors combined in different packages: a)

dipole-sextupole package for the arc cells and b) dipole / skew-quadrupole package for DS cells. Two possible design approaches, nested vs. lumped coil arrangement, and two different superconductors have been studied [23]. The lumped approach was chosen as the most simple and effective for magnet fabrication and correction system operation. It is expected that all correctors included in spool pieces will be powered from individual power supplies. To simplify the power supply and current lead designs, as well as corrector quench protection, the operational current of correctors was limited to 100 A. Since the operational temperature varies from 4.5 to 5.5 K, corrector temperature margin is a critical issue. NbTi and Nb_3Sn were compared in providing maximum corrector strength with sufficient critical current margin and sufficient temperature margin. It was found that NbTi can provide sufficient operational margin. Based on this and taking into account the availability of well-developed technologies for NbTi multipole correctors, they were chosen as a baseline approach for Stage-2 corrector magnets.

The cross-sections of the dipole, quadrupole and sextupole correctors are shown in Figure 6.11. Corrector operational parameters are summarized in Table 6.5.

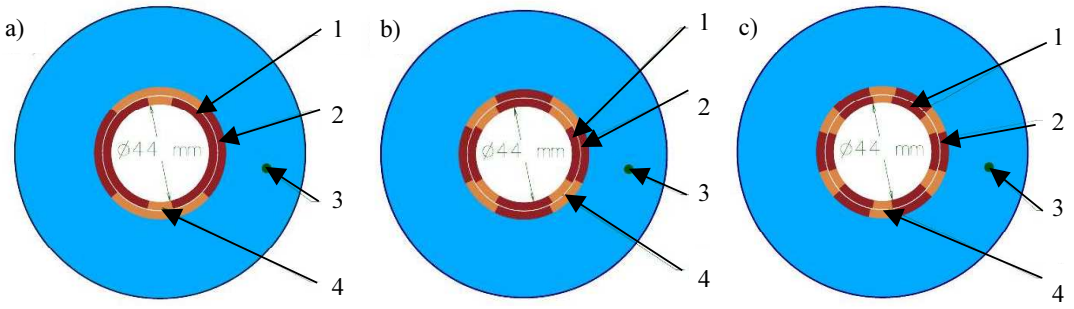

Figure 6.11. Dipole (a), quadrupole (b), and sextupole (c) corrector cross-section. The bore diameter for all 3 magnets is 44 m. 1 – coil (Δr_{coil}=2×3.6 mm); 2 – insulation (Δr_{ins} =0.5 mm); 3 – iron yoke (R_{in}=30 mm, R_{out}=65 mm); 4 – pole piece.

All coils have a two-layer design. In order to simplify the coil winding and optimize the coil packing factor, a flat single-layer ribbon cable is used having the parameters listed below. After coil fabrication, strands are connected in series to provide the required low nominal operation current. The strand and cable parameters are:

- Bare strand diameter - 0.3 mm
- Insulated strand diameter - 0.36 mm
- Cu/nonCu ratio – 2:1
- Jc(12T, 4.2K) – 2.75 kA/mm^2 (SSC)
- Number of strands – 10
- Width – 3.6 mm
- Mid thickness – 0.36 mm
- Insulation – 0.025 mm

Table 6.5. Stage-2 corrector parameters.

Parameter	Sextupole (n=2)	Quadrupole (n=1)	Dipole (n=0)
Required integrated strength, T-m/cm^n	0.74	0.95	2.3
Critical current I_c(4.2K), A	150	136	155
Nominal operation current I_{nom}, A	55	50	40
Critical current margin I_c/I_n	2.7	2.7	4.3
Critical temperature margin $\Delta T_c=T_c$-5.5, K	1.5	1.5	2.5
Nominal strength, T/cm^n	0.8	1.0	2.2
Magnetic length, m	0.93	0.95	1.1
Inductance L, H/m	1.4	2.5	5.4
Stored energy @10A, J/m	70	126	271
Current density in Cu matrix, A/mm^2	1167	1061	845

The main correction elements (dipole and sextupole coils or dipole and quadrupole coils) are combined in packages with a total length of ~2 m and placed in spool pieces near each quadrupole in the arc and DS cells. Adjacent to each arc focusing quadrupole spool piece are horizontal dipole and focusing sextupole windings. Adjacent to each arc defocusing quadrupole there is a spool piece with vertical dipole and defocusing sextupole windings. Spool pieces in DS cells consist of dipole and normal or skew quadrupole windings. Other correctors required in special regions of the Stage-2 arc could be combined with the main correctors and installed in the same corrector assembly.

6.1.5 IR Magnets

There are two possible approaches to the collision optics in Stage 2: one is symmetric doublet optics suited for the flat beams and the other is traditional anti-symmetric optics suited for round beams. The layouts of IR doublets and triplets, as well as the discussion of these two approaches from the accelerator physics viewpoint and machine luminosity considerations, are presented in Chapter 3.

The parameters of various IR magnets required for flat beam optics are summarized in Table 6.6. As can be seen from this table, the magnet parameters are very challenging. Achieving them will require development of innovative magnet designs and new superconducting and structural materials with unique properties. Some possible approaches to this problem are discussed in Section 10.2. The parameters of various IR magnets required for the case of round beam optics are summarized in Table 6.7.

The single bore separation dipole D1 is similar to the Nb_3Sn separation dipole magnet with 80-mm bore being developed for the second generation of the LHC IR [7]. In the vertical bore arrangement chosen for Stage-2 in this study, this magnet has to provide a horizontal field of 10 T. The other separation dipole D2 is a double bore magnet with a horizontal field in each aperture of 10 T. This magnet could be a modification of the arc dipole magnet based on the cos-theta design shown in Figure 10.4. Quadrupoles Q4, Q5, Q6 and Q7 are double bore magnets with the same cross-section and nominal field gradient as the arc quads but different magnetic length.

Table 6.6. Design parameters of Stage-2 interaction region magnets (flat beam optics).

Magnet	Field, T	Gradient, T/m	Aperture, mm	Length, m	Type
D1A	16	-	25	12.1	Single bore
D1B	12	-	50	6.0	Single bore
D2	12	-	50	11.1	2-in-1
Q1A	-	400	30	12.4	2-in-1
Q1B	-	600	30	12.4	2-in-1
Q2A	-	600	30	7.9	2-in-1
Q2B	-	600	30	7.9	2-in-1

Table 6.7. Design parameters of Stage-2 interaction region magnets (round beam optics).

Magnet	Field, T	Gradient, T/m	Aperture, mm	Length, m	Type
Q1	-	400	60?	23.58	Single bore
Q2a, Q2b	-	400	60?	18.98	Single bore
Q3	-	400	60?	23.58	Single bore
D1	10	-	80?	?	Single bore
D2	10	-	40?	?	2-in-1
Q4	-	400	40	10.47	2-in-1
Q5a, Q5b	-	400	40	15.09	2-in-1
Q6a, Q6b	-	330	40	15.09	2-in-1
Q7	-	375	40	10.47	2-in-1

The most challenging magnets are the inner triplet quadrupoles. These magnets should provide the same nominal field gradient of 400 T/m as the arc quads but in a significantly larger aperture. Scaling the parameters of the large aperture quadrupole magnet described in Section 5.1.4.1, one can see that the required field gradient of 400 T/m could be achieved in the two-layer quadrupole design with an aperture of 60 mm or larger using cable with similar or better parameters. Good field quality in these magnets is realizable. The 60-mm aperture should be sufficient for the required beam separation determined by the beam sizes and crossing angle as well as for the insertion inside the magnet an absorber. The absorber should be able to intercept a sufficient amount of the radiation-induced heat load at temperature higher than nominal in order to reduce the heat load on the IR cryogenic system.

The IRs will also contain a number of corrector magnets. The higher order harmonic correctors will be based on multi-layer coils within the same cold mass. These correctors will use Nb_3Sn superconductor to provide large operational margins (critical temperature and critical current) required in the IR with the high level of radiation heat deposition.

6.1.6 Cryostat and Spool Pieces

The cryostat serves to support the magnet cold mass, thermal shield(s) and cryogenic piping within the vacuum vessel, and to insulate the cold mass from heat radiated and conducted from the environment. It must function reliably during storage, shipping and handling, normal operation, quenches, and seismic excitations, and must have affordable cost. The major components of

the cryostat are the vacuum vessel, thermal shields, multi-layer insulation, cryogenic piping, interconnections, and suspensions.

Figure 6.12 shows conceptual layouts of the arc dipole and quadrupole cryostats [24]. Both cryostats are 958 mm wide and 1012 mm high. Their lengths are approximately 17 m and 9 m and total estimated weights are 42 tons and 22 tons respectively. The DS magnets have similar cross-sections, but are obviously shorter and lighter.

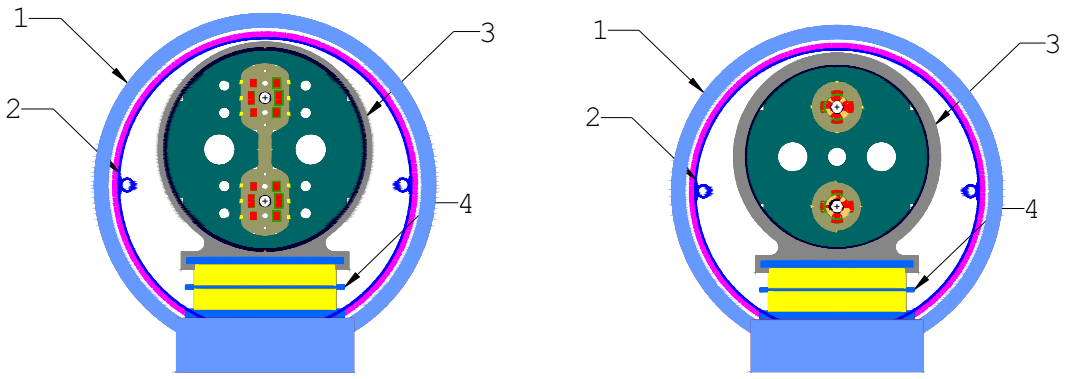

Figure 6.12. Stage-2 arc dipole (left) and arc quad (right) cryostat cross section: 1 – vacuum vessel; 2 – 80 K shield; 3 – cold mass; 4 – support post.

Table 6.8. Estimated static heat loads (W/m).

Temperature	80 K	4.5 K
Support conduction	1.5	0.3
Radiation and gas conduction	2.7	0.2
Total	4.2	0.5

Table 6.8 summarizes thermal design criteria for the Stage-2 arc magnet cryostats. The design shipping and handling load is 1 g, 2 g and 0.1 g in lateral, vertical and axial directions respectively. Magnet alignment criteria are similar to HERA, RHIC and LHC magnets.

The vacuum vessel contains the insulating vacuum, supports all other systems and serves also as a pressure containment vessel in the event of a failure in an internal cryogen line. The vessel is 914 mm OD with 12 mm wall. The length of the vacuum vessels will be determined as the lattice and interconnect requirements are finalized.

The cryostats have a single thermal shield cooled by He gas nominally at 80 K. The shields intercept heat radiated from the 300 K surface of the vacuum vessel and conducted through the support system. Aluminum extrusions serve as the supply and return for the shield flow. The shield itself is attached to the cryostat at the support structure. To minimize thermal gradients around the circumference the shell must have high thermal conductivity. Thermal analyses were performed using Cu and Al. Based on thermal analysis results and cost considerations the selected material is 6061-T6 Al, 3.175 mm thick. The shields are segmented along the length to minimize the effect of distortions during cooldown caused by the asymmetric cooling of the supply tubes. The shield extrusions are anchored at one of the magnet supports and are free to slide axially at the other to allow for thermal contraction.

The cold mass is covered by a single blanket of 10 layers of double aluminized Mylar separated by Nylon spacer material. The blankets are secured using Velcro strips. Similarly, two

blankets of 15 layers each will cover the 80 K shield. Two blankets are used to stagger the longitudinal seams.

Table 6.9 lists the sizes for each of the cryostat pipes. The pressure and flow parameters are reported in Section 6.2.1.

Table 6.9. Cryostat pipe sizes.

Description	OD (mm)	ID (mm)	Thickness (mm)	Notes
Vacuum vessel	914.0	890.0	12.0	Carbon steel
Dipole cold mass	580.0	560.0	10.0	Including outer shell
Quadrupole cold mass	542.0	530.0	6.0	Including outer shell
4.5 K supply	88.9	85.6	1.651	2 at each end dome
80 K shield supply	38.1	31.8	3.175	Aluminum extrusion
80 K shield shell	830.0	823.7	3.175	Aluminum shell

The suspension system serves as the structural attachment for all cryostat systems to the vacuum vessel, which in turn anchors them to the support platform. The design emphasis was on meeting the allowed suspension system conduction heat load, satisfying the structural requirements, and maximizing the suspension stiffness. The conceptual designs for the Stage-2 arc dipoles and quadrupoles uses support posts similar to those developed for SSC dipole cryostats and to those employed in LHC arc dipoles and quadrupoles. These supports are easy to manufacture, very strong and provide good thermal resistance to minimize heat load to the cold mass. Figure 6.12 conceptually illustrates cross-sections that utilize this support.

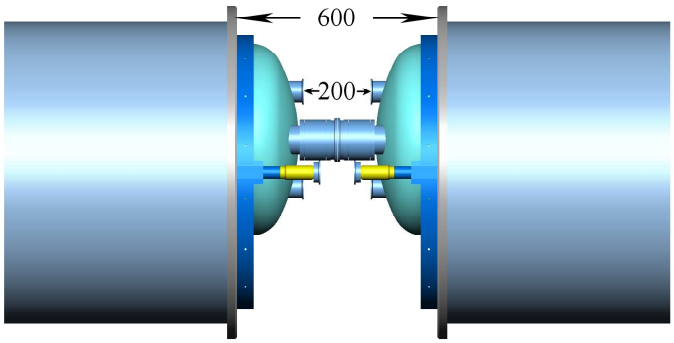

Figure 6.13. Dipole cryostat interconnect.

Figure 6.13 illustrates the interconnect of two arc or DS dipoles. The beam screen and electrical bus connections are not shown . One of the challenges of the interconnect is the beam screen connections between magnets. The details of these connections are unclear at this time, but necessitate connection of large number of small tubes carrying cold He gas at high pressure. Each pipe is anchored axially near the center of the magnet assembly.

In the case of a 17-m long dipole this means the interconnect bellows need to accommodate approximately 50 mm of axial cooldown contraction for stainless steel assemblies like the cold mass and 70 mm for aluminum assemblies like the thermal shield. Bellows are required on each cold mass, shield, and cryogenic pipe to allow for this expansion. Bellows are either hydroformed or welded stainless steel. Generally hydroformed bellows are used except where electrical connections requiring greater access are made up between magnets. In these locations welded bellows offer greater flexibility. For the aluminum extrusions on the shield, aluminum to stainless steel transition joints are required for the bellows connection. Lateral instability is a concern for interconnect bellows and requires the use of internal squirm protectors on each bellows assembly.

Shield bridges that span the gap between adjacent magnets minimize the radiative heat transfer in the interconnect area. These bridges are extensions of the magnet shields, modified to contain their respective bellow ODs if necessary. A sliding joint between bridge sections on adjacent magnets accommodates contraction during cooldown. Each is covered with the same multi-layer insulation (MLI) used throughout the body of the magnet. Each shield bridge also has a pressure relief to prevent pressure buildup in the event of an internal piping failure. They are located in the upper half of the shield sections in order to prevent liquid spills from impinging directly onto the vacuum vessel wall.

A spool piece is required at the end of each arc quadrupole to house the corrector packages, provide access to the cryogenic transfer lines, and a variety of other service-related functions. A preliminary list of spool requirements is shown below:

- Corrector package - 2 in each spool piece
- Corrector leads - 2 pairs of 100 A HTS leads per corrector
- Beam separation same as dipole and quadrupole *after* cooldown
- Vacuum break - every other spool
- Cross connection to transfer lines and warm pipes
- Vacuum pumpout ports - insulating and beam vacuums
- Vacuum gauge connections
- Instrumentation - thermometers for LHe and shield, pressure taps
- One 90 mm LHe pressure relief
- Vacuum relief
- HTS dipole (25 kA) and quadrupole (30 kA) power leads.

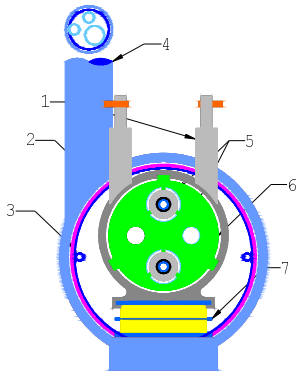

Figure 6.14. Spool piece cross-section. It consists of 4 pairs of HTS current leads (1), vacuum vessel (2), 80 K shield(3), connection to transfer line (4), corrector packages (5), cold mass support spider (6), and support post (7).

The spool piece cross-section is shown in Figure 6.14. The nominal length of a normal spool is 2.5-3 m. Spools will exist in several varieties, e.g. with and without vacuum breaks, with and without high-current dipole and quadrupole leads, etc. However, they will share many common design features with other spools and with the arc magnets. A preliminary design goal is to utilize as many features of the dipoles and quadrupoles as possible. The preliminary design shown in Figure 6.14 utilizes the same vacuum vessel and shield cross sections and the same support geometry as the arc magnets.

6.1.7 Magnet Quench Protection

The large energy stored in SC magnets is dissipated after quench in the normal zones, heating the coils and producing a voltage drop between the turns and between the coil and ground. Quench heaters installed in the magnet help to distribute this energy deposition throughout the coil, protecting it from overheating and preventing insulation damage from the high voltage and thermo-mechanical stress.

The maximum temperature and voltage were arbitrarily set to 300-400 K (similar to the LHC): 1000 V to ground and 100 V turn to turn. The high current density in the Cu-matrix of the conductors, requires effective quench detection, quick heater operation and a fast current decay in order to keep peak temperatures below the limit. The quench protection analysis is based on a quench detection time of 5 ms and a heater delay time of 35 ms. To provide such a short delay time the heaters are placed in the high field regions and cover almost 100% of the coil. The results of quench protection calculations for the arc magnets are summarized in Table 6.10; the details are reported in [25,26].

Table 6.10. Calculated quench characteristics.

Parameter	Arc Dipole	Arc Quad
QI(300K), MA^2s	42	40
QI(40 ms), MA^2s	22	30
T_{peak}, K	350	400
T_{bulk}, K	125	100
$V_{cg,}$ V	240	125
$V_{tt,}$ V	40	63
Decay time τ, ms	106	80

Analysis shows that the maximum temperature under heaters T_{bulk} in both magnets is less than 150 K. The maximum hot spot temperature T_{peak} is in the range of 350-400 K. The maximum turn to ground voltage V_{cg} is far from 1 kV and maximum turn-turn voltage V_{tt} is less than 100 V. Thus all magnet quench parameters are within the acceptable limits.

The heaters used in Stage-2 magnets are similar to the LHC dipole heaters [27]. One heater for the arc dipole consists of two stainless steel strips 15 mm wide, 25 μm thick, and 17 m long connected in parallel. One heater for the quadrupole consists of two 15-mm wide, 25-μm thick, and 10-m long stainless steel strips connected in series. To reduce the maximum voltage applied to quench heaters, they are periodically covered along their length with copper layers. The stainless to copper ratio is 1:3 (1 regular heater segment of the twist pitch length followed by a copper coated section of 3 twist pitch lengths). In the dipole case, 8 heaters are placed on the inner edge of the coil. In the quadrupole case, 4 heaters are placed between the two layers.

Table 6.11. Heater power supply parameters.

Parameter	Arc Dipole	Arc Quad
C_{tot}, mF	19	9.4
U_{tot}, V	1000	1000
U_{op}, V	700	700
E_{op}, kJ	4.6	2.3
Decay time, s	0.052	0.058
Peak current, A	252	113
Peak power, W/cm^2	138	111

Heater power supply parameters are given in Table 6.11. Each power supply for the dipole heaters consists of 16 capacitors (4.7 mF, 500V each); 8 sets of 2 series capacitors are connected in parallel. Each power supply for the quad heaters consists of 8 capacitors (4.7 mF, 500V each); 4 sets of 2 series capacitors are connected in parallel.

For a total insulation thickness of 0.5 mm between the heater and the cable, the heater heats the cable edge to 11.5 K after 35 ms [27]. At currents below the nominal, the heater delay time for a given peak temperature in the magnet increases such that the same heater will be able to induce a quench. The total number of capacitors for the arc dipole protection hardware is 128 or 2.5 times the amount of capacitors in the LHC. In the case of the arc quadrupole 64 capacitors are required.

Dipoles and quadrupoles in dispersion suppressor cells have the same cross section as arc dipoles and quadrupoles but slightly different length. Analysis shows [25] that the arc magnets can operate within the above limitations for a length up to 20 m. Based on that, quench protection of dipoles and quads in dispersion suppressor cells will be provided by the same method as for arc magnets.

Since corrector magnets will be powered from individual power supplies their protection will be provided by using low voltage power supplies with internal dump resistors. The quench protection scheme for the IR magnets will be developed later when IR magnet design and parameters are determined.

6.1.8 Magnet Production and Testing

Stage 2 will require ~11,400 (+ spare) double aperture dipoles, ~1700 (+ spare) double aperture quadrupoles, and about 1700 spool pieces with ~11,000-13,000 (+ spare) correctors of different types. To be able to fabricate all these magnets in 5 years the average production rate must be at least 3000 magnets per year or 8-12 magnets per day. This is an order of magnitude higher than the planned production rate for the LHC (and also for HERA and RHIC). The high production rate will require participation in the Stage-2 magnet production of many large, medium and small industrial companies.

The large number of superconducting magnets will require procurement of large amounts of superconductor and structural materials. The dipole magnets will require ~50,000 km of cable or ~3,300,000 km (9,500 metric tons) of 0.7-mm Nb_3Sn strand. The quadrupole magnets will require ~10,000 km of cable or ~300,000 km (1,300 metric tons) of 1-mm Nb_3Sn strand. Different magnet designs utilize ~45,000 tons of stainless steel (w/o cryogenics) and ~350,000 tons of iron (including cryostat). The superconductor volume (or cost) is thus the major parameter that will affect the cost and schedule of magnet and accelerator construction.

Before installation, all magnets go through quality control procedures, production tests and pre-installation tests. Production tests in industry include:

- magnetic and electrical measurements of all collared coils at room temperature
- magnetic and electrical measurements of all cold masses at room temperature
- final warm magnetic, electrical measurements, vacuum and pressure tests, geometry control of all fully assembled magnets in cryostats at room temperature

Pre-installation tests at Fermilab include control geometry, magnetic and electrical parameters after transportation, and magnet cold tests.

Standard measurement techniques and equipment will be used for the production and pre-installation tests. To provide these tests at an acceptable rate, both the magnet production factories

and the VLHC Laboratory have to be equipped with precise measurement apparatus and skilled personnel consistent with the machine construction schedule. To test ~13,000 dipoles and quadrupoles during 5 years will require an average test rate of 2600 magnets per year. Assuming a turn-around time per test bench and per double aperture magnet of 200 h (as for LHC) and 7200 working hours (300 days) per year, 73 cold test stands will be required. This number is a factor of 4.5 larger than expected for LHC magnet tests. The number of cold test stands could be reduced if a high reproducibility of main magnet parameters is achieved. Then only (~10-20%) of the magnets will have to be cold tested.

6.1.9 Magnet Installation, Including Survey and Alignment

The magnet installation procedure includes magnet transportation from storage to final position in tunnel, magnet placement and alignment, interconnection of individual magnets, vacuum and electrical tests, and survey. Installation of the large number of magnets requires systems and techniques that minimize cost and labor while preserving high accuracy and reliability. Taking into account that sizes and weights of the Stage-2 magnets are close to those of LHC magnets, and that the VLHC tunnel cross section is similar to LHC , the installation procedures, machines and tools similar to LHC will be used for Stage 2.

In order to reduce the time and cost of magnet installation, removal procedures and installation tests, significant attention at this stage was concentrated on the simplification of the magnet interconnect design, especially the optimization of the number of splices as well as the number and parameters of interconnecting pipes.

6.2 Accelerator Systems

There are many systems issues which a complete Stage-2 design needs to consider, including RF, cryogenics, vacuum, power supplies, instrumentation, feedback and controls, operational scenarios and safety systems. For this report, we report on studies performed on three key systems: cryogenics, discussed in Section 6.2.1; vacuum, including details of the beam-screen and photon-stops, described in Section 6.2.2; and the final section discusses magnet power supply and quench protection issues.

6.2.1 Stage-2 Cryogenic System Concept

6.2.1.1 Introduction

This study of possible high field VLHC cryogenic systems relies heavily on previous reports about VLHC cryogenics by M. McAshan and P. O. Mazur [28,29,30]. Comparisons are frequently made with LHC parameters not only because it is the most recent large accelerator cryogenic system design, but because the thorough analyses done in support of the LHC cryogenic system provide an excellent baseline for comparison. One of the most extensively used LHC documents was Ref. [31].

6.2.1.2 System Layout

The high field VLHC design effort will use 12 cryogenic plant locations as the working assumption for the cryogenic system layout. Such an arrangement creates 24 cryogenic strings of approximately 9.7 km length each.

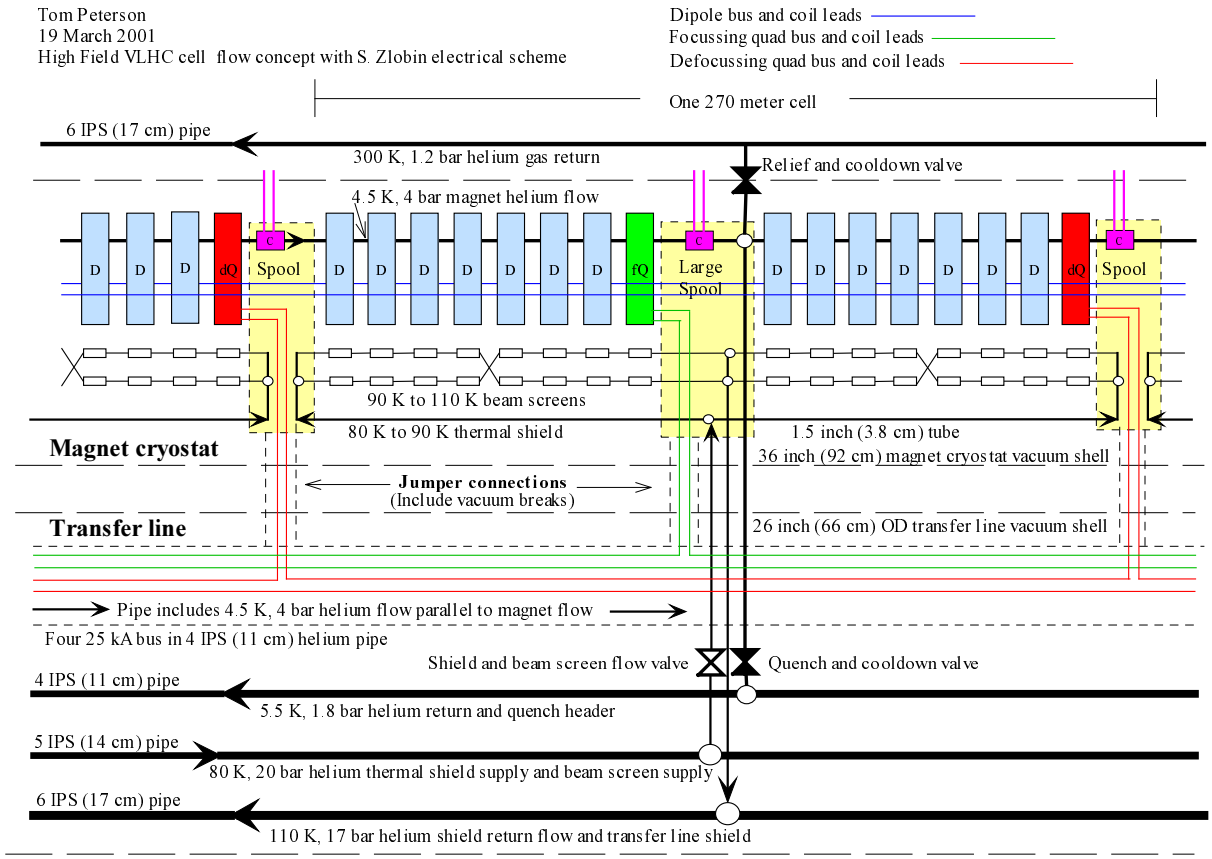

Figure 6.15. VLHC high field cryogenic schematic for one cell.

Shown in Figure 6.15 is a concept for a flow and electrical bus schematic for one cell of the high field VLHC. We avoid the use of recoolers or two-phase helium by allowing a 1 K rise in the helium flow through the magnet cold mass. Magnets are cooled by a large flow rate of supercritical, 4.5 K helium.

A nominally 80 K to 110 K helium stream cools the thermal shields and beam screens. High pressure (20 bar) helium is selected for the shield and beam screen since the higher pressure and density permit more mass flow in a given pipe size. Nevertheless, pressure drops for the 80 K to 110 K flow should be small so that most of the pressure remains available for expander work upon returning to the cold box.

This flow scheme provides four parallel beam screen cooling flow paths in each cell, two in each 135 meter long half-cell. A crossover is shown in each half-cell. The alternative to the crossover is balancing valves controlled by temperature sensors in the spool piece. Depending on how the beam screen passes through the interconnect, valves might be less costly than the crossover, but for now we will show the crossover.

This scheme puts all the large cold pipes and most of the electrical bus in a separate transfer line, so one does not have to deal with them at each magnet interconnect. It requires one jumper from the transfer line to the magnet string every 270 m for helium pipe connections, and one jumper every half-cell, or every 135 m, for electrical bus connections. Jumper connections containing electrical bus will require flow plugs to prevent helium flow short-circuits. The helium pipe containing four 25 kA bus may be cooled with a fraction of the 5.5 K, 1.8 bar return flow or with a parallel supply flow of 4.5 K, 4 bar helium. A 300 K helium gas return pipe is shown for lead flows and relief valve flow collection. A 300 K, 20 bar, helium gas line (not shown in Figure 6.15) might be required for inventory management.

The quench valve spacing of one every 270 meters appears to be adequate based on an analysis of quenching in 25 kA Nb_3Sn magnets [32]. Large quench valves would be required, with a port size of at least 60 cm, but quench pressures would remain under 20 bar.

All of the lines utilize helium as the coolant. Our initial decision is not to use nitrogen in the tunnel, but one might make good use of it above ground for cool-down and load leveling. Although it presents safety problems for the tunnel, one might reconsider the use of nitrogen in the tunnel in the thermal shields and/or for recooling helium from the beam screens, in order to reduce the huge helium inventory of this system.

6.2.1.3 Estimated Heat Loads

The heat load numbers in Table 6.12 are scaled from LHC heat loads as reported in Reference [31]. A thermal model [33,34,35] scales static heat loads to the thermal shields and cold mass for VLHC based on LHC experience. The synchrotron radiation heat load estimate comes from beam dynamics studies (Section 6.2.2 and Reference [38]). An analysis finding optimum beam screen temperature is also reported in [38].

The heat load to the thermal shield of the arc magnets in LHC at nominally 60 K is 3.7 W/m. Scaling to our high-field Nb_3Sn magnet concept, we find 4.2 W/m as the predicted static heat load to the VLHC magnet thermal shield. To the LHC transfer line at 60 K, the heat load is 2.7 W/m. Our VLHC transfer line is smaller in diameter than the LHC transfer line by 0.80, so we use $0.80 \times 2.7 = 2.2$ W/m to the transfer line thermal shield.

For the magnet cold mass heat load estimate, static and dynamic heat loads for LHC scale up with our higher current and higher luminosity in VLHC, adding 0.15 W/m to the 0.35 W/m LHC number, yielding 0.50 W/m for VLHC. In addition, we have a warmer beam screen than LHC, adding another 0.33 W/m (total for two beams), for a total of 0.83 W/m.

To the beam screen we estimate 10 W/m total for both beams due primarily to synchrotron radiation. Image current heating and multipacting are negligible compared to the 5 W/m/beam synchrotron radiation. As indicated in Figure 6.15 and in Table 6.12, the beam screen operational temperature in this flow scheme is between 87-107 K, at the predicted optimum range. Studies [35] have shown the optimal magnet thermal shield temperature (in terms of minimizing overall refrigeration power) to be about 63 K, consistent with the LHC selection of thermal shield temperature. In order to reduce the number of pipes through this VLHC system, the thermal shield and beam screen are placed in series with the thermal shield first. The high heat load on the beam screen results in its optimum temperature dominating that for the screen and thermal

shield combined. Thus, the optimum thermal shield average temperature when in series with the beam screen is 83 K.

Table 6.12. Predicted heat loads and power requirements.

		Shield supply pipe (in transfer line)	Thermal shield (magnet)	Beam screen (two beams)	Shield return pipe and thermal shield (transfer line)	Magnet cold mass
Temp in	(K)	77.00	77.61	87.58	77.61	4.5
Press in	(bar)	20.0	19.4	19.3	18.1	4.0
Temp out	(K)	77.61	87.58	106.58	108.82	5.5
Press out	(bar)	19.4	19.3	18.1	17.7	1.8
Predicted heat load	**(W/m)**	**0.1**	**4.2**	**10.0**	**2.2**	**0.83**
Heat uncertainty factor		1.25	1.25	1.00	1.25	1.25
Design heat load	**(W/m)**	**0.13**	**5.25**	**10.00**	**2.75**	**1.04**
Distance	(m)	9700.0	9700.0	7824.0	9700.0	9700.0
Design total heat	(kW)	1.2	50.9	78.2	26.7	10.1
Design mass flow	(g/s)	1104.0	13.6	6.8	1104.0	422.7
Design ideal power	(kW)	10.4	137.5	194.5	63.0	647.3
4.5 K equiv design power	(kW)	0.2	2.1	3.0	1.0	9.9
Efficiency (fraction Carnot)		0.30	0.30	0.30	0.30	0.30
Efficiency in Watts/Watt	(W/W)	28.7	9.0	8.3	7.9	214.4
Nominal operating power	(kW)	34.8	458.2	648.5	210.1	2157.6
Overcapacity factor		1.30	1.30	1.30	1.30	1.30
Installed operating power	(kW)	45.2	595.7	843.0	273.1	2804.8
Percent of power		1.0%	12.6%	17.9%	5.8%	59.4%

Total installed operating power for one 10 km string (MW)	4.7
Total installed 4.5 K equivalent power for one 10 km string (kW)	21.2

Number of above "strings" in accelerator	24
Operating wall plug power for cryogenics for entire accelerator (MW)	**85.7**
Installed wall plug power for cryogenics for entire accelerator (MW)	**113.3**
Installed 4.5 K equivalent power for entire accelerator (kW)	508.9
Installed number of LHC system equivalents	3.5

6.2.1.4 Current Leads

There is one 25-kA dipole circuit per 10-km string and two 25-kA quadrupole circuits per 20 km. The 25-kA dipole circuit requires a pair of current leads at each end of the 10-km string. Thus, each cryo plant location has eight 25-kA leads and each 10-km turnaround point has 4 leads. We assume six 100 A corrector leads per beam per spool piece, with about 75 spools in one 10-km sector, for a total of 900 corrector leads per sector. LHC current lead test data [36] and Fermilab HTS lead test data [37] were used to scale cooling requirements for Stage-2 current leads. The relatively low number of high-current leads and the use of HTS leads make the total cooling power for the current leads only about 4% of the cryogenic system power. Lead details are not shown in Table 6.12, but lead cooling power is included in the totals in the table.

6.2.1.5 Cooling Power Requirements and Plant Sizing

Table 6.12 shows that the heat load estimates and the 233-km circumference of the VLHC give rise to a system requiring about 113 MW of installed cooling power, equivalent to about two large cryoplants at each of the 12 locations. Such a system would total about 3.5 times the cooling capacity of the LHC cryogenic system. Note the applied factors: the uncertainty factor of 1.25 on heat loads other than the beam screen, the Carnot efficiency of 0.30 which is high but achievable with today's technology (LHC reports 0.3 for their helium systems), and the overcapacity factor of 1.3. Overcapacity is the cooling capacity reserve required for availability, maintenance, control, and non-optimal operation. LHC uses a factor of 1.5. We have reduced that to 1.3 in light of the large proportion of heat load due to synchrotron radiation, over which we have control.

6.2.1.6 Cool-Down and Warm-Up

Cool-down times are estimated to be on the order of two months using liquefier capacity. Each 20 km of high field VLHC has roughly 35,000 tons of cold mass (about equal to LHC), requiring the removal of about 3×10^{12} Joules to cool to 80 K. Some reduction in time can be gained with the use of above-ground LN_2 precooling, but extremely large amounts of LN_2 storage would be required. The extremely large cold mass will force long cool-down and warm-up times. "Warm iron" magnets could offer significant advantages in reducing cool-down and warm-up times and hence system repair times and system availability.

6.2.1.7 Helium Inventory

The inventory for the entire machine is estimated to be 0.65 million kg or 5 million liquid liters equivalent. This is about 85 times the Tevatron inventory, 7 times the LHC inventory, and about 0.056 of the annual U.S. production of helium, costing about $12 million. We found in this study that one of the problems with reducing the number of cryogenic plant sites from 12 to 6 is that doubling the lengths of cryogenic loops, along with doubling the mass flow to maintain the same exit temperature, requires significantly larger diameter pipes. As a result, the helium inventory for such a system is approximately twice this one, about 10 million liquid liters instead of 5 million liquid liters. Twenty-four 10 km magnet strings might not be precisely the optimum division of the Stage-2 cryogenic system, but we believe it is closer to the cost optimum than twelve 20-km strings.

6.2.1.8 Conclusions and Recommendations

The large total system power, the magnet string lengths, total cold mass, and total helium inventory for a Stage-2 cryogenic system go well beyond that of previous systems. This cryogenic system is technically feasible in that the required machinery assembled into smaller, similar systems exists. But system design and optimization on this scale will require significant effort and R&D.

Recommendations for cryogenic system R&D may be found in Section 10.2.4. One particular area of R&D, removal of synchrotron radiation at room temperature, deserves special mention. At $0.114/kWh, power would cost $1.00 per Watt-year, so the "installed power" shown in MW could be approximately the annual power bill in M$. Thus, one can see that it would be

very desirable to reduce the installed power to significantly less than the presently estimated 113 MW. The heat load with the biggest potential for reduction by some innovative method is probably the synchrotron radiation. Developing methods for removing some significant fraction of the synchrotron radiation at room temperature could permit a dramatic reduction in cryogenic system size (both power and inventory) for a high field VLHC.

6.2.2 Vacuum System

6.2.2.1 Synchrotron Radiation

With a proton energy of 87.5 TeV and a bending radius of 29.9 km, the critical energy of the synchrotron radiation emitted by the protons is 8 keV, which corresponds to a wave-length of ~1.6 Å. At a peak current of 57.4 mA each beam releases 4.7 W/m and 1.2×10^{16} photons/sec/m in the bending magnets. The total synchrotron radiation power emitted by the two beams is 9.4 W/m. This, combined with additional heat load contributions such as resistive wall power loss and emittance growth-related loss due to multipactoring electrons and ion-induced desorption – estimated to total <1 W/m/beam, would be an excessive heat load for the cold mass. Thus, a beam-screen, maintained at a higher temperature by a flow of gaseous helium, is inserted inside the magnet cold bore to intercept this power.

The synchrotron radiation photons impinging on the beam-screen desorb gas molecules from the near surface layer and convert them into a steadily increasing surface density of loosely bound (physisorbed) states. These physisorbed surface molecules are easily redesorbed by the photons, deteriorating the quality of the vacuum in the beam chamber. Therefore, the beam-screen will be perforated over a few percent of its surface, to allow cryopumping to the 5 K cold bore surface, where the vapor pressure of all gases (except H_2 and He) is negligible and the condensed gas is shielded from synchrotron radiation and ion bombardment.

6.2.2.2 Beam-Screen Cooling

6.2.2.2.1 Optimum Beam-Screen Temperature

The cooling of the beam-screen is a key issue in the VLHC. The beam-screen refrigeration power requirement is the leading contributor to the total cryo-budget. The beam-screen refrigeration power requirement is a strongly varying function of the beam-screen operational temperature. The optimum beam-screen temperature balances between the heat load absorbed by the beam-screen refrigeration system and the heat load absorbed by the cold mass. At low beam-screen temperature, the heat load is absorbed mainly by the beam-screen, at low thermodynamic efficiency and thus at high cost. For a high beam-screen temperature, the cost of beam-screen refrigeration is reduced, but a significant part of the heat load is transferred from the beam-screen by conduction and radiation to the cold mass, where it is extracted with low thermodynamic efficiency. The thermodynamic optimum beam-screen temperature in Stage-2 was calculated to be 86 K [38] for the case of 5 W/m/beam.

The baseline Stage-2 cryo-concept (Section 6.2.1) foresees that the beam-screens are cooled in series with the cold-mass thermal shield by the same high pressure helium gas. Although both systems have different optimum operational temperatures when separated, the optimum (aver-

age) operating temperature of the cold mass thermal shield in the combined system is 83 K, and the ensuing average beam-screen temperature is 98 K. At this temperature the beam-screen refrigeration system requires a total wall plug power of 15 MW (both beams). In these conditions the heat load transferred from two beam-screens to the cold mass is 0.26 W/m (conduction) and 0.07 W/m (radiation). At a cold mass temperature of 5 K, the evacuation of the heat load transferred from both beam-screens to the cold mass represents a wall plug power requirement of 14.4 MW for the complete ring.

6.2.2.2.2 Concept for a Beam-Screen Cooling System

Following a calculation procedure outlined in [38], the beam-screen cooling system requires ~12% of the area enclosed by the cold bore (ID=34 mm), or 110 mm^2 in cross-sectional area, to be taken up by the coolant at an average temperature of 100 K. The coolant is high pressure gaseous helium, entering the beam-screen cooling system at 87 K, 19 bar and exiting at 106 K, 18 bar. The beam-screen cooling system length is assumed to be the length of a half-cell (135 m). The total flow rate per beam-screen is 6.6 g/s. In the calculations the stainless steel cooling duct wall thickness was assumed to be 0.5 mm.

6.2.2.3 Vacuum

6.2.2.3.1 Synchrotron Radiation

The high photon flux is the dominant source of gas-desorption. On the other hand, it is very effective in cleaning the exposed surfaces via photo induced desorption. The use of superconducting magnet technology results in the amenity of a low cold bore temperature of ~5 K, at which most gases have a very low saturation vapor pressure. Therefore, most gases get trapped at the cold bore walls and remain there until the magnets are warmed up again to room temperature. The pumping capacity of such a cryo-pump is very large and compatible with the accelerator lifetime. In addition, the high beam-screen temperature decreases the rate of re-adsorption of gas on the beam-screen and thus facilitates the cleaning process. The higher saturation vapor pressure of H_2 at 5 K on the other hand results in the limitation that H_2 cannot be cryo-pumped beyond one monolayer. Therefore the cold bore will have to be warmed up to room temperature at regular intervals (some years) to allow regeneration of the cryo-pumping surfaces.

6.2.2.3.2 Residual Gas Pressure

The residual beam-tube pressure must be low enough to limit beam-gas scattering to a level at which the lifetime of the beam is not significantly affected, and at which the radiation into the magnet cold mass remains below a stipulated limit. Estimations of the bounds on the beam tube gas pressure for the most common UHV gases are listed in Table 6.13. The beam lifetime limiting pressure is calculated, stipulating that the beam-gas scattering lifetime be five times larger than the luminosity lifetime (7.5 hours). The beam lifetime reduction stemming from beam-gas scattering related emittance growth is neglected because of strong radiation damping. The limiting pressure to restrict the power radiated into the magnet cold mass due to beam-gas scattering is calculated, stipulating that the beam-gas scattering power be less than 0.1 W/m/beam. According to the table, the limiting pressure in the VLHC has to be in the nTorr range for the most common UHV gases.

Table 6.13. Numerical bounds on the beam tube gas pressure for the most common UHV gases in Stage-2, calculated for each gas "alone" at ambient room temperature equivalent pressure.

Gas	Max pressure for a beam gas scattering lifetime of 5 × 7.5 hours (nTorr)	Max pressure for a beam gas scattering power of 0.1 W/m/beam (nTorr)
H_2	31.8	50.3
CH_4	5.9	9.3
H_2O	5.5	8.7
CO	3.8	6
CO_2	2.4	3.8

6.2.2.3.3 Photo Desorption and Pumping Speed

Photo-induced desorption due to synchrotron radiation with a critical energy of 8 keV is the most important source of vacuum contamination in the Stage-2 VLHC. Calculations based on procedures formerly developed in [39], have recently [40] been performed to estimate the quantity of gas desorbed by synchrotron radiation from a copper coated beam-screen. Copper can be prepared (baked) to have a small initial photo-desorption coefficient η_0 (e.g. ~0.0035 H_2 molecules per photon) which offers the advantage of a low secondary electron emission coefficient (reducing the electron cloud effect). It is believed that the initial photo-desorption coefficient does not increase further with the critical energy of the photons, above a few keV, a range for which reliable measurements exist [41].

The photo-desorbed gas load has to be matched by a pumping speed to remain within the specified pressure bounds. The CO equivalent pumping speed required to keep the heat dissipation in the magnet below 0.1 W/m after one third of an operational year ($I \cdot t$ = 48 A-hours) is 5.6 lit/sec-m. For H_2 this pumping speed is 21 lit/sec-m. During the commissioning phase of the machine the photo-desorption rate is larger, requiring a larger pumping speed and/or a smaller beam current. A possible commissioning beam- current profile (for a CO equivalent pumping speed of 61 l/sec-m) was proposed [40]. The current in the profile is calculated for the condition that the beam-gas scattering power always remains below 0.1 W/m. It consists of three 15 hour cycles with initial currents of 30 mA, 38 mA and 54 mA. The total conditioning time is thus 45 hours.

6.2.2.3.4 Cryo-Pumping

Due to its low saturation vapor pressure, H_2 cannot be cryo-sorbed on a 5 K surface beyond one monolayer (~3×10^{15} H_2/cm^2). Pumping speeds of 61 lit/sec-m, as required for conditioning (see above), can be achieved through cryo-pumping the gas onto the cold (5 K) magnet bore. The beam-screen surface fraction occupied by pumping slots to obtain 60 lit/sec-m is ~1.5 %. The integrated gas-load set free by the synchrotron photons during a 20 year accelerator operation is ~1.1×10^{19} H_2 molecules/m. This represents 3.3 mono-layers of H_2. This gas-load can be managed by periodic warm-up of the machine to allow regeneration of the cryo-pumping surfaces.

6.2.2.4 Conceptual Beam-Screen Design

We propose a vacuum system design (Figure 6.16), similar to the LHC design [42], using a perforated liner operating at ~100 K. Beam-stability issues related to the "higher" temperature of the beam-screen are being investigated. The beam-screen is a 1-mm thick non-magnetic stainless steel (μ_r<1.005) tube with a round cross-section, flattened top and bottom. The space between it and the surrounding cold bore contains the cooling pipes carrying the forced flow supercritical helium. The pipes, e.g., made of stainless steel, are laser welded to the beam-screen. The beam-screen is centered within the cold bore by steel/bronze rings, every 0.5 m. The assumed magnet bore ID is 40 mm. A 1.5-mm gap is needed to allow the insertion of the cold bore into the magnet. Then, to withstand the quench-pressure, the cold bore tube needs a wall thickness of 1.5 mm, hence the cold bore inner diameter becomes 34 mm. The supports require an additional 0.75-mm gap between the cold bore and the beam-screen. The remaining aperture for the beam-screen becomes 32.5 mm. The inner dimensions of the beam-screen are 30.5 mm in width and 20 mm in height.

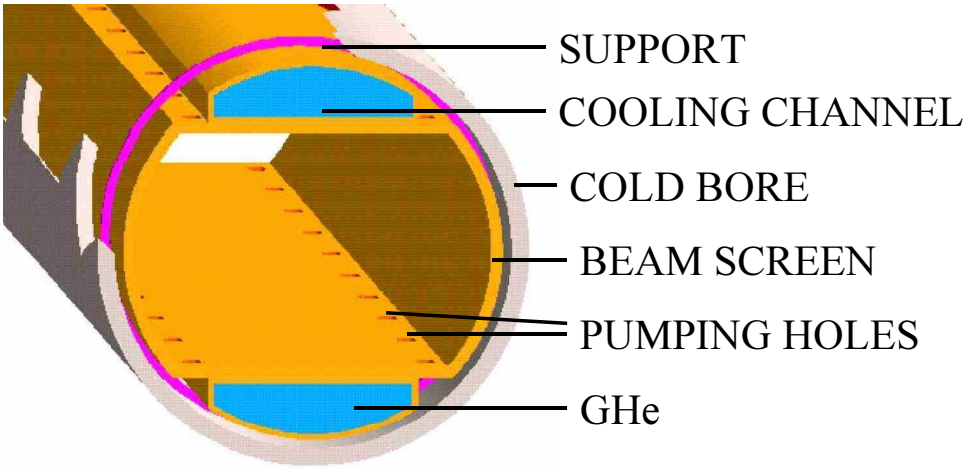

Figure 6.16. A schematic view of the beam-screen showing supports, cooling pipes and pumping slots.

To minimize resistive wall heating and longitudinal beam impedance the interior surface of the screen is covered by a thin co-laminated layer of high purity copper. The pumping slots are rounded (1.5 mm wide, 8 mm long)) and randomly distributed to reduce beam-coupling impedance and resonance effects. To obtain a pumping speed of 60 lit/sec-m, 120 holes are required per meter of beam-screen (e.g. 4 rows of 30 holes, one hole every 5 cm). As in the case of LHC [42] the beam-screen is fabricated from sheet metal with stamped cooling slots. It is cold-rolled with the copper foil and cold-pressed into the shape of a half tube, which is then welded together. To eliminate the effects of heat load variations between the apertures, the cooling tubes should cross-over to the other aperture at every half cell (as proposed in Section 6.2.1).

6.2.2.5 Photon-Stops

6.2.2.5.1 Justification

The strong synchrotron radiation in Stage-2 results in a refrigeration power requirement of ~25 MW. Intercepted at room temperature, the synchrotron radiation heat load would represent a reduced power at the plug of ~1.9 MW. Motivated by the considerable cost saving potential, the use of room temperature operated photon-stops, which are commonly used in synchrotron light sources [43], is under evaluation. Photon-stops are devices that protrude into the beam tube at the end of each bending magnet and scrape off the synchrotron light beam emitted in the second magnet up-stream from their location. A preliminary feasibility study was recently performed [44], showing that, given the arc bending radius in the VLHC of 29.9 km, it is possible to place photon-stops between the magnets with a length and aperture compatible with the current VLHC design. We believe that synchrotron radiation in the VLHC is a sufficiently serious issue to justify the use of both a traditional beam-screen as well as photon-stops. In the case that the photon-stops are retractable, the synchrotron heat load can be shared in a controlled way between both systems which would allow operation of the accelerator at energies and luminosities above nominal.

6.2.2.5.2 Geometrical Issues

A geometrical model was based on the assumptions that 1) the bending magnets are straight and positioned such that the average distance between the ideal particle orbit and the magnet center is always minimal, and 2) all particles are moving very close to the ideal orbit. The model estimates the maximum permissible magnet length and the minimum distance between the photon-stop and the beam. Given that the photon-stops are placed at the beginning of the 3-m long straight section between the magnets and a 30-mm horizontal beam-screen aperture, the maximum permissible bending magnet length is 14 m, which is compatible with the maximum magnet length imposed by quench protection and transportation constraints. In this condition, the synchrotron radiation emitted from the beginning of the second up-stream magnet will heat the photon-stop at its base (where it enters the beam tube) and the radiation emitted from the end of the same magnet will hit its tip. The SR emitted by the magnet up-stream from the photon-stop passes through the gap between the photon-stop tip and the beam. The emission angle of the SR is approximately $1/\gamma \sim 10$ μrad. The total radial extension of the photon-stop is 1 cm, such that its (minimum) distance from the particle orbit becomes ~5 mm.

6.2.2.5.3 Engineering Design

Assuming that a single photon-stop intercepts the synchrotron radiation heat load emitted by one beam over the length of one magnet, the thermal load is given by ~5 W/m times the magnet-length of 70 W. The required heat exchange surface is ~1 cm^2 at a coolant flux of 0.2 liter/sec, given a cooling tube wall thickness of 1 mm and a cooling tube diameter of 10 mm [45]. The coolant assumed in this calculation is water at room temperature; the coolant temperature rise is 5 K. The peak heat flux of 0.6 MW/m^2 remains safely below the critical heat flux of forced flow water (~5 MW/m^2). The largest SR power fraction is transported by photons with a wavelength of 0.5 Å. The radiation length of steel, used as a reference material in the thermal calculation, is ~0.04 g/cm^2 or 0.05 mm. The synchrotron radiation hits the absorber in a ~0.5-mm (rms) thin strip. The absorber surface material needs sufficient thermal conductivity and thickness to

distribute the heat load over a larger area to dilute the surface heat flux density to the coolant. Heaters, wrapped around the cooling tubes, are required to prevent the cooling liquid from freezing when no synchrotron radiation heat load is present. A preliminary engineering design that satisfies these thermal considerations was presented [45].

According to this design, the photon-stop is a T-shaped piece, consisting of a ~6 cm short copper tube shaped like the beam-screen (but without pumping slots) with flanges at the ends, to which a ~0.5 m long warm finger, the photon-stop, is attached perpendicularly. The photon-stop enters the beam-screen from the side, where it is hit by the synchrotron radiation (Figure 6.17).

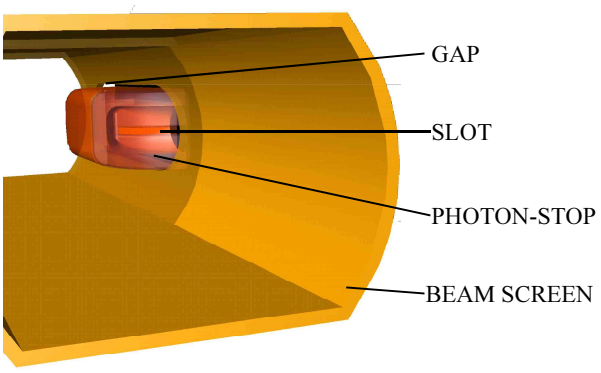

Figure 6.17. Photon-stop sketch according to the engineering design proposal.

The photon-stop assembly consists of an outer hull with flanges on top and bottom to fix it to the cryostat hull and the short beam-screen piece with vacuum tight seals. Into this hull the core of the photon-stop is inserted. The core piece consists of the cooling tubes with the radiation absorber at the end. The short beam-screen piece is inserted into a specially prepared gap in the beam-screen / cold-bore assembly and welded at each end. The cold-bore tube is discontinued over the ~10 cm of the photon-stop to reduce the heat influx from the 100 K beam-screen / photon-stop system.

The bellows, required to allow the beam tubes to contract during magnet cool-down, are placed in sections further away from the photon-stop. The beam-screen cooling tubes have to be guided out of the beam-screen to bypass the bellows, usually in the form of flexible tubes. For the photon-stop we propose that the cooling tubes also bypass the photon-stop system. Furthermore, it is assumed that the photon-stop will be placed close to the magnet anchoring point. This offers the advantage of not having to cope with longitudinal thermal contraction effects.

At the heart of the photon-stop is the radiation absorber, a hollow cylinder machined at one end into a special shape. The inside of the end piece is hollow to allow the cooling liquid to extract the heat deposited by the synchrotron radiation on its outer surface. The wall thickness of the absorber is ~ 2 mm. It is made from copper to obtain a low initial photo-desorption coefficient and high thermal conductivity. To reduce the thermal emissivity and the photo-desorption coefficient, the outer surface of the end piece requires a high grade polishing. The shape of the absorber was optimized to yield low impedance. It has the shape of a prism (Figure 6.17), with axial / radial / azimuthal extensions of 35 × 10 × 10 mm with respect to the beam tube, and rounded edges.

A major issue regarding the absorber is scattering of the low energy (long wavelength) spectrum of the SR. Measures aimed at the reduction of the scattered photon-fraction have to be pursued. One possibility, for example, is to make the absorber piece hollow, with an entry slot for the photons. For such a photon-catcher to be efficient, a more detailed knowledge of the geometrical characteristics of the photon beam is required.

6.2.2.5.4 Photon-Stop Impedance

The longitudinal impedance of the photon-stop has to be small to 1) reduce the impedance related power loss per turn, and 2) avoid beam instabilities, such as the microwave instability. The transverse impedance has to remain below beam instability thresholds, such as for the transverse mode coupling instability (TMCI). A major issue is whether the photon-stops can be treated as independent. In the coupled case the sum of the impedances of all coupled devices would be the relevant parameter, and thus the impedance limitations would be more stringent. A first estimation of the coupling strength can be obtained from the damping length of the first order mode. The damping length was calculated [46] to be 4.2 cm, which is sufficiently smaller than the projected distance between the photon-stops of ~14 m, such that coupling is suppressed.

The beam tube impedance of a copper coated, round beam tube (ID=30 mm) is of the order of a few ohms. The cut-off frequency of such a pipe is $2\pi \cdot 7.6$ GHz, which is larger than the largest characteristic beam frequency in the VLHC, the bunch-length frequency at collision of $2\pi \cdot 5.8$ GHz. A simple, analytical model to calculate the impedance of a "half ellipsoidal" protrusion in the beam pipe [47] predicts, for a total number of 14500 photon-stops and a longitudinal extension of the protrusion of 3.5 cm and a radial/azimuthal extension of 1 cm, the longitudinal impedance Z_{II}/n becomes 25 mΩ. The transverse impedance for all photon-stops together becomes $Z_{\perp}$=8 MΩ/m.

An estimate [46] of the microwave instability threshold bunch population is 3×10^{12}, two orders of magnitude larger than the Stage-2 bunch population. Numerical wake calculations, using MAFIA© [46], indicate a TMCI threshold bunch population of 4.5×10^{11}, still larger than the design peak number of protons per bunch. We believe that the photon-stops will not cause TMCI.

Trapped modes are of concern in cavity-like structures, e.g., holes in the beam pipe and sharp edges. We believe that photon-stops, with the appropriate design, will not be a major cause of trapped modes.

The impedance calculations were performed assuming that the photon-stops are made of copper and have indicated the viability of this concept. Another possible approach to the design of this device would be the use of dielectric materials with low electrical permittivity and high thermal conductivity, such as sapphire or diamond. Although this approach would be advantageous from an impedance standpoint, complications are expected to arise in conjunction with the removal of surface charge and the lack of knowledge of the photo-desorption coefficients. In addition these solutions could be more expensive.

6.2.2.5.5 Photon-Stop Vacuum Issues

The strong synchrotron radiation flux impinging on the photon-stop results in a fast clean-up of the photon-stop surface. However, it is necessary to pump the desorbed gas load. According to the engineering design proposed, the beam-screen in the photon-stop system has no pumping holes. The desorbed gas load has to diffuse ~5 cm to each side into the beam tube to reach sections where active pumping to the cold-bore removes the gas from the beam area. The high temperature of the photon-stop (~350 K) and the beam-screen (~100 K) certainly prevents re-adsorption of the desorbed gases and thus the pumping task is simplified. The high surface temperatures result as well in a high molecular speed, accelerating the gas diffusion into the adjacent beam-screen regions, where the pumping occurs. On the other hand the high

temperature of the photon-stop raises the thermal desorption rate. Vacuum simulations are required to determine if the longitudinal diffusion is sufficient to ensure a proper vacuum in the photon-stop sections. It will certainly be necessary to perform a high temperature heat treatment (bake-out) of the photon-stop insert before installation.

6.2.2.5.6 Photon-Stop R&D Issues

An R&D plan has been presented, that lists the most important tasks on the path toward the realization of a photon-stop for Stage-2 VLHC [48]. These tasks include 1) a detailed investigation of the characteristics of Stage-2 SR to allow for an optimization of the absorber shape, 2) continued impedance calculations to improve the understanding of the effects of the photon-stop on beam stability, especially with the use of improved absorber shapes aimed at a reduction of the photon scattering rate, 3) vacuum simulations to investigate the magnitude of the pressure bump in the photon-stop sections and to calculate a suitable conditioning profile, 4) (warm) testing of prototypes in a synchrotron source photon beam, 5) cryo-testing of the prototypes, and finally 5) full blown vacuum tests in a Stage-2 vacuum system mock-up exposed to SR, as have been performed for the SSC and LHC projects.

6.2.3 Magnet Power Supply and Quench Protection

6.2.3.1 Stage-2 Electrical schemes

Arc dipoles and short straight section quadrupoles will be grouped into electrical circuits ordered for efficient electrical distribution, space utilization, and minimization of cryogenics and cooling water requirements. Power supplies for these circuits will be located in ground level service buildings at 12 feeder locations corresponding to the cryogenic plants (Section 6.2.1). Circuit boundaries will match cryogenic boundaries; this will enable 1/12 sections of the ring to be commissioned independently, and will also sectorize the maximum quench load on the system. Additional low current supplies will be required for corrector magnets. Finally, power supplies are needed to energize quench protection strip heaters for the superconducting dipole and quadrupole circuits.

6.2.3.2 Arc Dipole and Quadrupole Power Schemes

The arc dipoles (Section 6.1.1) will be powered in 24 circuits, 2 circuits per feeder location as shown in Figure 6.18. Each circuit will consist of approximately 450 dipoles in series with a 25 kA power supply, a reference magnet for monitoring the field harmonics, and an energy extraction system. The characteristics of each circuit are shown in Table 6.14.

The twin dipole apertures will be internally bused in series, with a cold bypass diode across the magnet terminals to electrically isolate the magnet in the event of a quench. Each circuit will have two room temperature extraction resistor banks, located symmetrically in the circuit. One bank will be located near the power supply, while the other bank will be located in an alcove halfway between the feeder access ports. Each bank is capable of dissipating ~3 GJ of stored energy. The resistance and location of the extraction circuits determine the peak voltage to ground as well as the discharge time of the circuit. Limiting the peak voltage to ±1 kV requires

two 85 mΩ dump resistors. Using the LHC dipoles circuits as a scale, each circuit will require 9 times the LHC energy extraction.

Power supply requirements depend on the total stored energy, and the current vs. time profile used to reach the peak operating field. With a constant ramp rate, 150 MW of power will be required for the 2000 second ramp to the operating field of the dipole circuits. Using a "constant power" ($I = K\sqrt{t}$) time vs. current profile reduces the peak power consumption by a factor of two, but puts an unacceptably large voltage requirement on the dipole power supplies and increases the accelerator RF power requirements at lower currents. A linear ramp (constant RF accelerating voltage) followed by a "constant power" ramp looks like an attractive compromise. The break between the linear and constant power portion of the ramps can be optimized based on the relative cost of supplying RF and dipole current power.

The quadrupoles will be divided into 24 circuits. As shown in Figure 6.19, focussing and defocusing quadrupole circuits will be separated to facilitate tuning. The focussing- defocusing circuit pair covers 1/12 of the accelerator and is matched to two dipole circuits and a corresponding cryogenic supply. A single extraction circuit for each quadrupole circuit will be located in the power supply service building. As shown in Table 6.15, the power supply and extraction requirements are modest compared to the dipole circuitry.

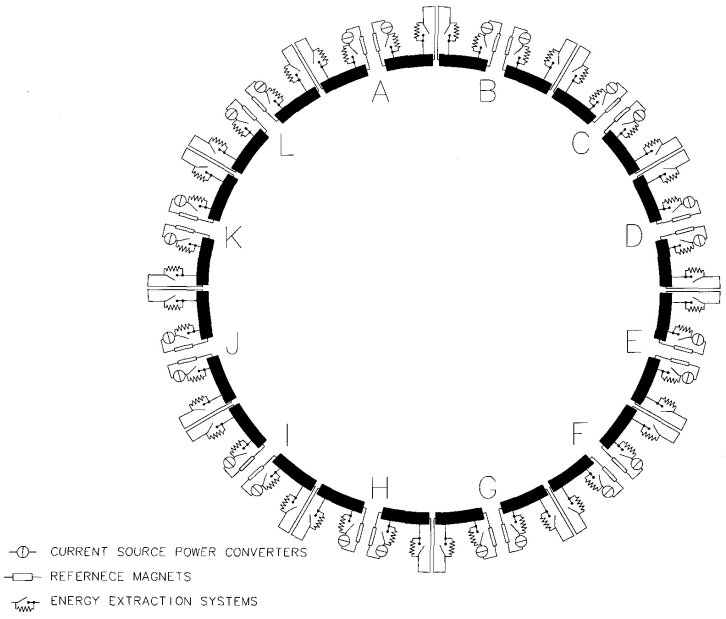

Figure 6.18. Electrical distribution for dipole circuits. Power supplies are located in ground level service buildings A-L.

Table 6.14. Dipole circuit.

Number of magnets	450
Circuit Inductance (H)	22.95
Stored energy (GJ)	6.34
Operating Current (kA)	23.50

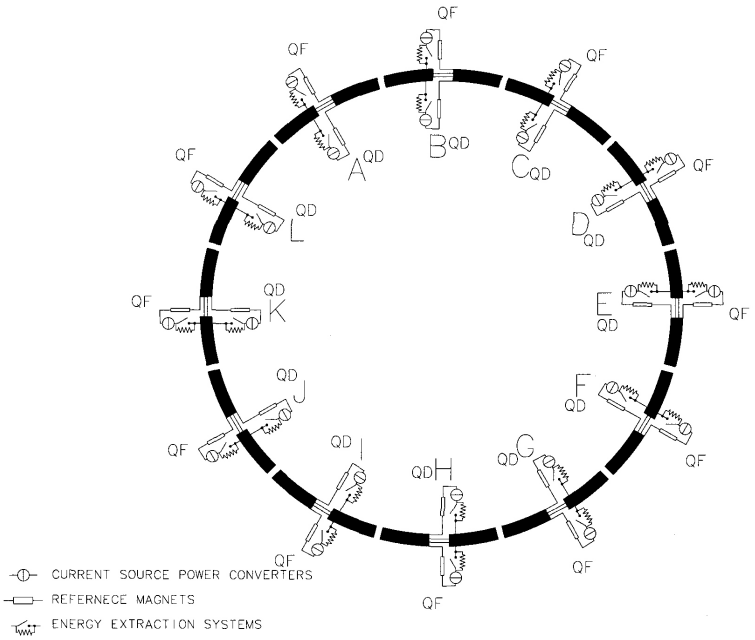

Figure 6.19. Electrical distribution for arc quadrupoles.

Table 6.15. Quadrupole circuit.

Number of Magnets	65
Circuit Inductance (H)	0.65
Stored energy (GJ)	0.30
Operating Current (kA)	25.00

6.2.3.3 Corrector Powering

The correctors required for Stage-2 are described in Section 3.5 and in Section 6.1.4. Dipole, quadrupole and sextupole correctors will be packaged into spool pieces and will be locally powered. Currents will be less than 100 amps. Power supplies should be kept as close as to the spool pieces as possible, space and radiation permitting to reduce the power loss in the leads.

6.2.3.4 Bus work

The dipole and quadrupole bus work will consist of superconductor stabilized with copper. The amount of copper is sized to protect the bus for excessive temperature in the event of a bus quench. Based on the LHC dipole experience, the required copper cross section for the dipole and quadruple bus would be ~900 mm^2 and 200 mm^2 respectively. Dipole bus will likely be placed inside the magnet coldmass. Unlike the dipole bus, the two quadrupole buses could be routed through an auxiliary bus port parallel to the dipole/quadrupole cold mass but inside the cryostat. It is then possible to have these buses as a continuous piece spanning many contiguous cryogenic elements, simplifying the bus manufacturing and eliminating several splices. The bus configuration is shown in Figure 6.15.

6.2.3.5 Quench Protection Powering

Quench protection strategy centers around the use of strip heaters. Strip heaters are thin copper clad stainless steel strips that are in good thermal contact with the coils. Banks of capacitors are discharged into the heaters in order to quench the coils and thus distribute the quench energy more uniformly throughout the dipoles and quadrupoles. Studies have been performed in order to determine the required heater coverage and power supplies. The power supplies for the dipoles quadrupoles are comparable in voltage and capacitance (within a factor of 2.5) of those require

for the LHC magnets [49]. The power supplies and quench detection electronics should be located as close to the magnets as possible, space and radiation limits permitting, to reduce quench detection signal noise as well as power loss in the heater leads.

References

[1] G. Ambrosio et al., "Development of the 11 T Nb_3Sn Dipole Model at Fermilab," *MT-16,* IEEE Transactions on Applied Superconductivity, v. 10, No. 1, March 2000, p.298.

[2] G. Ambrosio et al., "Development of React & Wind Common Coil Dipoles for VLHC," *ASC'2000*, IEEE Transactions on Applied Superconductivity, v. 11, No. 1, March 2001, p. 2172.

[3] S.A. Gourlay et al., "Design and Fabrication of a 14 T, Nb_3Sn Superconducting Racetrack Dipole Magnet," *MT-16,* IEEE Transactions on Applied Superconductivity, v. 10, No. 1, March 2000, p.294.

[4] S. Caspi et al., "Design of a Nb_3Sn High Gradient Low-beta Quadrupole Magnet," *MT-15*, Proceedings, Oct 20-24, 1997, Beijing, China, p.175.

[5] R. Gupta et al., "Common coil magnet Program at BNL," *ASC'2000*, IEEE Transactions on Applied Superconductivity, v. 11, No. 1, March 2001, p. 2168.

[6] T. Elliott et al., "16 Tesla Nb_3Sn Dipole Development at Texas A&M University," IEEE Transactions on Applied Superconductivity, June 1997, p. 555.

[7] A. den Ouden et al., "A 10 T Model Separator Magnet for the LHC," *MT-15*, Proceedings, Oct 20-24, 1997, Beijing, China, p.137.

[8] A. den Ouden & H. ten Kate, "Application of Nb_3Sn Superconductors in High-Field Accelerator Magnets," IEEE Transactions on Applied Superconductivity, June 1997, p. 733.

[9] A. McInturff et al., "Test Results for a High Field (13T) Nb_3Sn Dipole," Particle Accelerator Conference (PAC97), Vancouver, Canada, 1997, p. 3212.

[10] A. Lietzke et al., "Racetrack Coil Technology Validation (RT-1) Test Results," Proc. of 2nd VLHC Magnet Workshop, Fermilab, May 2000 (http://vlhc.org).

[11] R.M. Scanlan et al., "Conductor Development for High Field Dipole Magnets," *MT-16,* IEEE Transactions on Applied Superconductivity, v. 10, No. 1, March 2000, p.288.

[12] Superconducting Super Collider, Conceptual Design, SSC Central Design Group, SSC-SR-2020, March 1986.

[13] The Large Hadron Collider, Conceptual Design, The LHC Study Group, CERN/AC/95-05 (LHC), 20 October 1995.

[14] V.V. Kashikhin and A.V. Zlobin, "Magnetic Designs of 2-in-1 Nb_3Sn Dipole Magnets for VLHC," *ASC'2000*, IEEE Transactions on Applied Superconductivity, v. 11, No. 1, March 2001, p. 2176.

[15] I. Novitski et al., "Design and Mechanical Analysis of a Single-Layer Common Coil Dipole for VLHC," *ASC'2000*, IEEE Transactions on Applied Superconductivity, v. 11, No. 1, March 2001, p. 2276.

[16] E. Barzi et al., "Strand Critical Current Degradation in Nb_3Sn Rutherford Cables," *ASC'2000*, IEEE Transactions on Applied Superconductivity, v. 11, No. 1, March 2001, p. 2134.

[17] P. Bauer et al., "Fabrication and Testing of Rutherford-Type Cables for React and Wind Accelerator Magnets," *ASC'2000*, IEEE Transactions on Applied Superconductivity, v. 11, No. 1, March 2001, p. 2457.

[18] G. Ambrosio et al., "Superconductor Requirements for the HFM Program at Fermilab," Fermilab, TD-99-073, December 15 1999.

[19] E. Barzi et al., "Study of Nb_3Sn Strands for Fermilab's High Field Dipole Models," *ASC'2000*, IEEE Transactions on Applied Superconductivity, v. 11, No. 1, March 2001, p. 3595.

[20] V. Kashikhin and A.V. Zlobin, "Conceptual Designs of 2-in-1 Nb_3Sn Arc Quadrupole Magnets for VLHC," Fermilab, TD-01-019, March 2001.

[21] D. Chichili, "Mechanical Analysis of FF Arc-Quadrupole for VLHC Stage-2," Fermilab, TD-01-012, March 5, 2001.

[22] V.V. Kashikhin and A.V. Zlobin, "Correction of the Persistent Current Effect in Nb_3Sn Dipole Magnets," *ASC'2000*, IEEE Transactions on Applied Superconductivity, v. 11, No. 1, March 2001, p. 2058.

[23] A.V. Zlobin, TD note on VLHC-2 correctors.

[24] T. Nicol, "VLHC Arc Dipole and Quadrupole Cryostats," Fermilab, TD-01-016, March 2001.

[25] P. Bauer et al., "Quench Protection Calculations for Fermilab's Nb_3Sn High Field Magnets for VLHC – Part 1," Fermilab, TD-01-003, February 2001.

[26] P. Bauer et al., "Quench Protection Calculations for Fermilab's Nb_3Sn High Field Magnets for VLHC – Part 2," Fermilab, TD-01-004, February 2001.

[27] L. Imbasciati, G. Ambrosio, and P. Bauer, "Quench heater design considerations for VLHC magnets," Fermilab, TD-01-022, April 2001.

[28] M. McAshan and P. O. Mazur, "Cryogenic Systems for the High Field RLHC Study Cases," 1996 Snowmass Study.

[29] M. McAshan and P. O. Mazur, "Cryogenic Systems for the Low Field RLHC Study Cases," 1996 Snowmass Study.

[30] M. McAshan, "Cryogenic Systems for the 3 TeV Injector Study," VLHCPUB-87, Dec 1997.

[31] L. Tavian and U. Wagner, "LHC sector heat loads and their conversion to LHC refrigerator capacities," LHC Project Note 140 (1998).

[32] Roger Rabehl, VLHC quench study and "Cooldown of a VLHC-2 Magnet String," personal communications.

[33] C. Darve, A. Poncet, D. Willems, "CTM3, the latest evolution of the cryostat thermal model: thermal performance measurements of the first run from March to May 1998," Technical Note 98-19, 03/1999.

[34] C. Darve, G. Ferlin, M. Gautier, L.R. Williams, "Thermal performance measurements for a 10 meter LHC dipole prototype (Cryostat Thermal Model 2)," LHC-Project-Note-112, 11/1997.

[35] C. Darve, P. Bauer, T. Nicol, T. Peterson, "VLHC Thermal Shield Cooling," Fermilab Tech. Div. note TD-01-035, 2001.

[36] Amalia Ballarino and Albert Ijspeert, "Design and Tests on the 30 to 600 A HTS Current Leads for the Large Hadron Collider," CERN-LHC-Project-Report-78, 24 Oct 1996.

[37] G. Citver et al., "Thermal tests of 6-kA HTS current leads for the Tevatron," Advances in Cryogenic Engineering, Vol. 45B, (2000), pp. 1549 – 1556. (Also FERMILAB-Conf-99-284)

[38] C. Darve et al., "VLHC Beam-screen Cooling," Fermilab Technical Division Note TD-01-005, 02/01.

[39] W.C. Turner, "Beam Tube Vacuum in Low Field and High Field Very Large Hadron Colliders," LBNL-39482, UC 414, presented at the Snowmass Conference, Oct. 1996.

[40] P. Bauer et al., "Vacuum Calculations for the VLHC - stage 2," Fermilab, Technical Division Note, TD-01-011, 04/01.

[41] A. Mathewson, O. Groebner, P. Strubin, R, Marin, R. Souchet, AIP Conf. Proc., 236, 313, 1990.

[42] O. Groebner, "The LHC Vacuum System," Proceedings of the Particle Accelerator Conference 1997.

[43] S. Sharma et al., "High Heat-Load Absorbers for the APS Storage Ring," Proceedings of the 1st International Workshop on Mechanical Engineering Design of Synchrotron Radiation Equipment and Instrumentation, PSI-Wurenlingen, Switzerland, July 2000.

[44] I. Terechkine, "Synchrotron Radiation in the VLHC," Fermilab, Technical Division, unpublished note, 01/01.

[45] P. Bauer et al., "A Photon-stop for VLHC-2 – Engineering Design – Part 1," Fermilab, Technical Division Note, TD-01-023, 04/01.

[46] P. Bauer, N. Solyak, "A Photon-stop for the VLHC-2 – Impedance Calculations," Fermilab Technical Division Note TD-01-014, 04/01.

[47] S. Kurennoy, in M. Tigner, A. Chao, eds., "Handbook of Accelerator Physics and Engineering," World Scientific, 1998, p. 207.

[48] P. Bauer et al., "Photon-Stop R&D Plan," Fermilab Technical Division Note TD-01-030, 05/01.

[49] P. Bauer, L. Imbasciati, G. Ambrosio, V. Kashikhin, A. Zlobin, M. Lamm, "Quench Protection Calculations for Fermilab's Nb_3Sn High Field Magnets for VLHC, Part II," TD-01-004 FNAL (March 2001).